



Enhancement of band-gap characteristics in hexagonal and re-entrant lattices via curved beams

Shuvajit Mukherjee^{a,*}, Milan Cajić^{a,b,**}, Danilo Karličić^b, Sondipon Adhikari^c

^a Faculty of Science and Engineering, Swansea University, Bay Campus, Swansea SA1 8EN, UK

^b Mathematical Institute of the Serbian Academy of Sciences and Arts, Kneza Mihaila 36, Belgrade, Serbia

^c James Watt School of Engineering, The University of Glasgow, Glasgow G12 8QQ, UK

ARTICLE INFO

Keywords:

Hexagonal lattices
Curved beams
Timoshenko beams
Bloch waves
Phononic bandgaps

ABSTRACT

In-plane wave propagation in hexagonal and re-entrant lattices is a widely investigated subject in the literature. Such systems can exhibit many different but limited band structure properties that depend on the topology and geometry of structural members and the lattice itself. This manuscript proposes a novel class of hexagonal and re-entrant lattices with unit cells containing combined straight and curved beams with enhanced band-gap properties. Timoshenko beams are suggested to represent beam members of the lattice and corresponding governing equations are derived. Bloch theorem is applied to study in-plane wave propagation and get the unique dispersion properties of the modified lattices. The influence of a new geometric parameter, the curvature angle of the constituent curved beams is explored for the dispersion characteristics and wave directionality through iso-frequency contours of dispersion surfaces. Enhanced band-gap properties in the context of the generation of new band-gaps and widening of the band-gaps for the cellular lattices with curved beams are promising from the viewpoint of the future design of phononic crystals and metamaterials in their mechanical setup.

1. Introduction

Lattice structures are widely used in engineering practice due to their unique mechanical properties, robustness, and economic efficiency. These applications range from structural and civil engineering to crystallography, biological and material sciences [1]. An important requirement for some structural components is a lightweight design typically combined with increased stiffness, which can conflict with the need for energy-related dissipation of undesired vibrations and shock. In [2] the authors have shown that both of these requirements, load-carrying capabilities, and vibration attenuation, can be achieved through an embedded lattice with chiral configuration. Many authors have proposed a variety of lattice designs and investigated their wave propagation and dispersion properties. Most common one-dimensional [3] and two-dimensional designs include triangular and square lattices [4], hexagonal/re-entrant [5] and chiral lattices [6].

A comprehensive analysis of plane wave propagation and directional behaviour in hexagonal and re-entrant beam-based lattices was performed in [7]. Different band structures and directional properties were achieved for varying angles between beam members based on Bloch theory, dispersion relations, phase, and group velocities.

Dispersion curves are usually plotted within the irreducible Brillouin zone, where approximate numerical methods are used to obtain dispersion relations based on the corresponding unit cell and constructed reciprocal lattice. The directional energy flow and stop band identification was also investigated for different types of lattices in [8] by proposing a method which produces group velocity maps. In [9] the author suggested an exact wave-based Bloch method to study wave propagation in the two-dimensional square, honeycomb, and hexagonal lattices, where predicted corresponding dispersion curves are compared and advantages emphasized against those obtained via finite elements. Despite interesting band structure properties, classical lattice structures often lack desired band-gap properties and there were many attempts in the literature to introduce modifications and improvements in lattice topology [10–14] towards this direction. For example, a novel design for honeycomb lattices with widen band-gaps was suggested by combining the conventional and auxetic cores [15]. Some authors [16] introduced the effect of pre-stress on beam elements in the hexagonal lattice to shift the band-gap to lower frequency. Band gaps can be also manipulated by changing the design of individual beam members or the unit cell geometry either manually or through the utilization of

* Corresponding author.

** Corresponding author at: Mathematical Institute of the Serbian Academy of Sciences and Arts, Kneza Mihaila 36, Belgrade, Serbia.

E-mail addresses: shuvajit.mukherjee@swansea.ac.uk (S. Mukherjee), mcajic@mi.sanu.ac.rs (M. Cajić).

topology optimization methods [17–19]. Timoshenko beams of non-uniform thickness [20] were employed in hexagonal and re-entrant lattice structures where widening of the existing ones and emerging of new band-gaps were noticed for certain ranges of material distribution parameters. Moreover, topological design based on the improved genetic algorithm was applied to the square lattice structure by filling the material to manipulate the lower frequency band-gaps [21]. Besides these straightforward methodologies, some authors suggested the application of fractal-inspired [22,23] or bio-inspired [24] lattice structures capable of inhibiting the wave propagation at sub-wavelength frequency ranges.

Another ambitious approach to control the band-gaps at both lower and higher frequency ranges includes lattices with zigzag and undulated geometry of limbs in the unit cell. Several types of two-dimensional beam-like zigzag lattice structures were proposed in [25, 26] and their band-gaps and directional wave propagation were investigated in detail. It was revealed that multiple wide and complete band-gaps appear in a wide porosity range due to the separation of the degeneracy when bending arms are introduced. Similarly, wave propagation analysis was performed for the triangular chiral lattice containing zigzag beams [27] and for the re-entrant and anti-chiral hybrid auxetic metastructures with mass inclusions [28]. Moreover, undulated geometry obtained by using the initial curvature to the square lattice elements was studied in [29]. The authors devoted special attention to induced anisotropy and break of symmetry to the regular square lattice, which resulted in band-gaps at specified frequency ranges as well as a wave motion in specific directions. Utilizing the fact that curved beams can perform a weaker stiffness and therefore exhibit lower band-gaps, a recent study [30] performed a wave propagation analysis of rotationally symmetric lattices with curved beams that are transformed from square lattices. Numerical simulations and experiments were conducted to demonstrate the existence of lower band-gaps and directional wave propagation when certain geometrical parameters are manipulated.

Motivated by previous studies [25,31–33], the influence of curved beam elements are explored for achieving lower and emergence of new band-gaps modifying the conventional hexagonal lattice. Here, attention has been paid to hexagonal and re-entrant lattices modified by curved beams. Flexibility and weaker stiffness properties of such lattices were demonstrated in a recent study [31]. Therefore, a unit cell composed of one straight and two curved beams approximated by many straight Timoshenko beams is proposed. Corresponding governing equations are derived and the finite element method and Bloch theorem are applied to obtain the dispersion relations, and investigate and compare the band structures of different curved beam configurations with the conventional one. Unlike the curved beam-based square lattice [30], where the unit cell is exhibiting a full rotation symmetry and has a limited number of emerging and vanishing bang gaps, in our case of modified hexagonal/re-entrant-like variation of curved beam geometry leads to the emergence, widening and even shifting of band-gaps to lower frequencies. The convergence study is performed to see what number of beams is required to approximate the curved beams with satisfying accuracy of eigenvalues. Moreover, the dispersion relations are given in the form of iso-frequency curves to investigate the amount of anisotropy in the wave propagation characteristic of the observed lattices. Today's additive manufacturing technologies allow us to design lattices with a variety of geometries which makes lattices with curved elements and desired wave propagation features easy to make and utilize in different engineering applications. The structures presented in this study give an insight into potential applications of curved lattices in the direction of mechanical filters, sound isolations, tunable acoustics, energy absorption, vibration control, and control and manipulation of wave propagation. Their main advantage lies in the emergence of new lower and higher frequency band gaps only by manipulating the angles of curved beam elements while keeping the main topological features of the lattice.

2. Wave propagation in two-dimensional lattice structures with curved beams

2.1. Mechanical model and geometry of a unit cell

Let us consider a two-dimensional lattice hexagonal/re-entrant-like type of lattice modified by curved beams, More precisely, a representative unit cell is composed of one straight and two curved beams as given in Fig. 1.

Four different combinations of lattices considering straight and curved beams, where curvatures are varied from one or another side of the straight configuration, are considered as illustrated in Fig. 1. However, it should be noted that in further analysis curved beams are approximated with a satisfying number of straight beams based on previously performed convergence analysis. Details about the geometry of the unit cell with its characteristic dimensions and base vectors are also given in Fig. 2. One can observe two characteristic angles of the unit cell elements, where θ is a cell angle which defines the angle between the inclined beam members and the axis normal to the straight beam element while ψ is the curvature angle (see Fig. 2). This means that taking the cell angle θ as a positive or negative value characterizes the lattice as hexagonal or re-entrant, respectively. Change of curvature angle ψ defines the amount of modification of a lattice from the hexagonal/re-entrant configuration. It is worth mentioning that lattice points of modified lattices are the same as in the conventional case and the basis vectors for the periodic unit cell are denoted as e_1 and e_2 . The entire lattice can be formed by tessellating the periodic unit cell in the direction of the lattice vectors. Thus, the wave propagation characteristics can be obtained by analysing a single unit cell by applying the Bloch theorem and periodic boundary conditions. The details about the lattice vectors and Bloch theorem are elaborated/explained in Appendix A and Appendix B, respectively.

2.2. Timoshenko's beam equations

The constituent beam members are modelled as the assembly of straight Timoshenko's beam. We consider the following material characteristics of the Timoshenko beam: ρ is the density, h is the beam width, E is the modulus of elasticity, $G = E/(2(1 + \nu))$ is the shear modulus while Poisson ratio is denoted as ν . We also adopted the shear correction factor as $k_s = 10(1 + \nu)/(12 + 11\nu)$. The governing equations for the Timoshenko beam are well known in the literature. However, for the sake of simplicity, we will repeat the derivation procedure based on Hamilton's principle. Therefore, the variations of the kinetic δK and potential δU energy are defined as

$$\delta K = \int_0^L [\rho A \dot{u} \delta \dot{u} + \rho I \dot{\zeta} \delta \dot{\zeta} + \rho A \dot{w} \delta \dot{w}] dx, \quad (1)$$

$$\delta U = \int_0^L \left[EA \frac{\partial u}{\partial x} \delta \frac{\partial u}{\partial x} + EI \frac{\partial \zeta}{\partial x} \delta \frac{\partial \zeta}{\partial x} + GA k_s \left(\zeta - \frac{\partial w}{\partial x} \right) \delta \left(\zeta - \frac{\partial w}{\partial x} \right) \right] dx, \quad (2)$$

where δ denotes the variation operator.

Using Eqs. (1) and (2) and Hamilton's principle gives

$$\int_{t_1}^{t_2} (\delta K - \delta U) dt = 0, \quad (3)$$

Finally, after performing the standard procedure one can get governing equations for the longitudinal and transverse vibrations of the Timoshenko beam as

$$\rho A \ddot{u} - EA \frac{\partial^2 u}{\partial x^2} = p(x, t) \quad (4)$$

$$\rho A \ddot{w} + GA k_s \left(\frac{\partial \zeta}{\partial x} - \frac{\partial^2 w}{\partial x^2} \right) = q(x, t) \quad (5)$$

$$EI \frac{\partial^2 \zeta}{\partial x^2} - GA k_s \left(\zeta - \frac{\partial w}{\partial x} \right) - \rho I \ddot{\zeta} = 0 \quad (6)$$

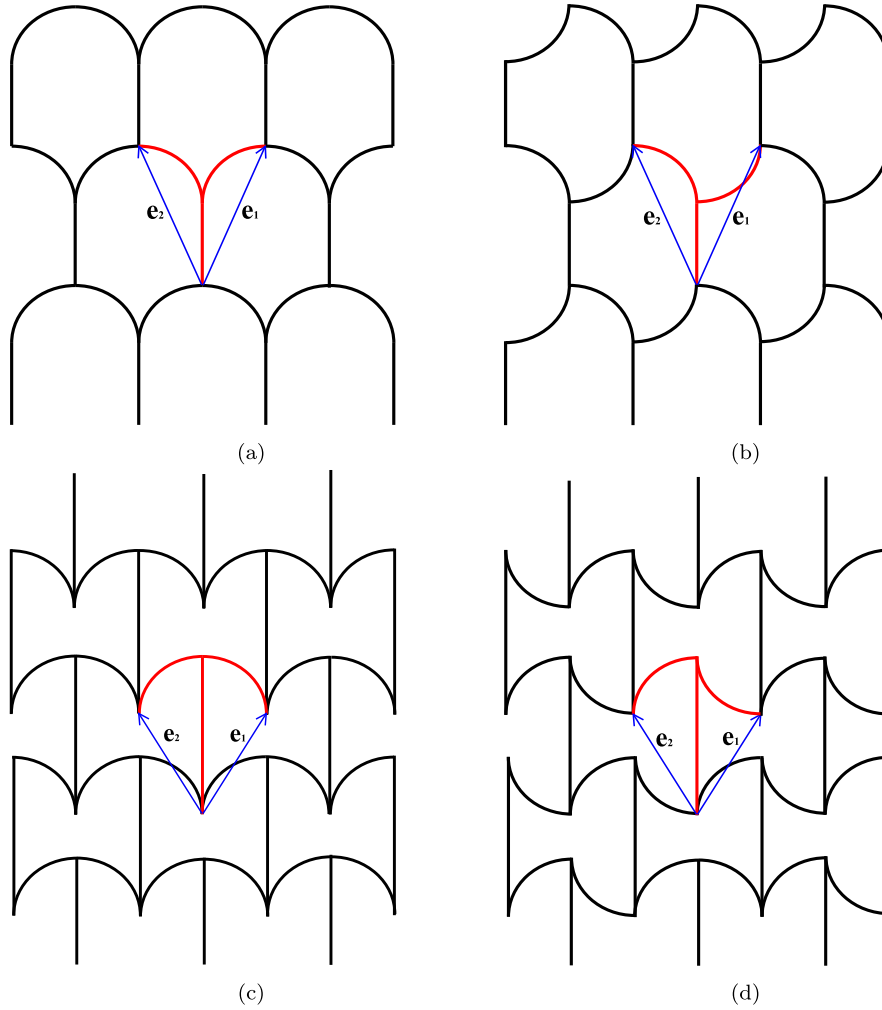


Fig. 1. Curved lattices and their corresponding unit cells along with the direct lattice vectors denoted as \mathbf{e}_1 and \mathbf{e}_2 . (a) curved hexagonal lattice, (b) curved hexagonal lattice with reverse curvature, (c) re-entrant curved lattice, (d) re-entrant curved lattice with reverse curvature.

where $w(x, t)$ denotes the transverse displacement, $u(x, t)$ is the axial displacement, and ζ is rotation of the cross section. We adopted that $(\dot{\cdot}) \equiv \partial(\cdot)/\partial t$. In this work we neglect the influence of the external axial $p(x, t)$ and transverse $q(x, t)$ loads.

2.3. The finite element formulation of the unit cell

Here, the finite element method is employed to discretize the governing equations of a unit cell with applied Bloch boundary conditions. As mentioned previously, a unit cell is given as an assembly of one rigidly connected straight beam with two inclined curved beams. Each beam is discretized by straight Timoshenko beam elements. The convergence analysis to obtain a minimum number of straight beams that can approximate the curved beam is given in Section 3.1.

Finite element models for Timoshenko beam are adopted in the same manner as in [34] with approximations of displacements $u(x, t)$ and $w(x, t)$ and rotation $\zeta(x, t)$ given as follows

$$u(x, t) = \sum_{j=1}^6 N_j^u(x) q_j(t), \quad w(x, t) = \sum_{j=1}^6 N_j^w(x) q_j(t), \quad (7)$$

$$\zeta(x, t) = \sum_{j=1}^6 N_j^\zeta(x) q_j(t),$$

where $N_j^u(x)$, $N_j^w(x)$ and $N_j^\zeta(x)$, ($j = 1, 2, \dots, 6$) represents the shape functions for six nodal degrees of freedom of the Timoshenko beam

element. The nodal vector is $\mathbf{q}(t) = [u_1, w_1, \zeta_1, u_2, w_2, \zeta_2]^T$. The shape functions used in this work are given in Appendix C. If we consider the governing equations for Timoshenko beam Eqs. (4)–(6), energy variation Eqs. (1)–(3) and approximation of displacements and rotation Eq. (7) we get

$$\mathbf{M}^e \ddot{\mathbf{q}}^e + \mathbf{K}^e \mathbf{q}^e = \mathbf{f}^e, \quad (8)$$

where \mathbf{M}^e is the finite and \mathbf{K}^e are mass and stiffness matrices of the beam element while \mathbf{q}^e and \mathbf{f}^e are the corresponding element displacement and force vector, respectively.

By considering a typical unit cell of a hexagonal and re-entrant lattice, the model represents a frame structure where mass and stiffness matrices (\mathbf{M}^e , \mathbf{K}^e) of the beam element are obtained in local coordinates but should be transformed into the global ones. In the following, the relation between the global and local mass and stiffness matrices is given

$$\mathbf{M}_g^e = \mathbf{T}^T \mathbf{M}^e \mathbf{T}, \quad \mathbf{K}_g^e = \mathbf{T}^T \mathbf{K}^e \mathbf{T}, \quad (9)$$

where the transformation matrix \mathbf{T} is given as

$$\mathbf{T} = \begin{pmatrix} \mathbf{T}_0 & \mathbf{0} \\ \mathbf{0} & \mathbf{T}_0 \end{pmatrix}, \quad (10)$$

and the rotation matrix \mathbf{T}_0 as

$$\mathbf{T}_0 = \begin{pmatrix} \cos \varphi(\psi, n, \theta) & \sin \varphi(\psi, n, \theta) & 0 \\ -\sin \varphi(\psi, n, \theta) & \cos \varphi(\psi, n, \theta) & 0 \\ 0 & 0 & 1 \end{pmatrix}, \quad (11)$$

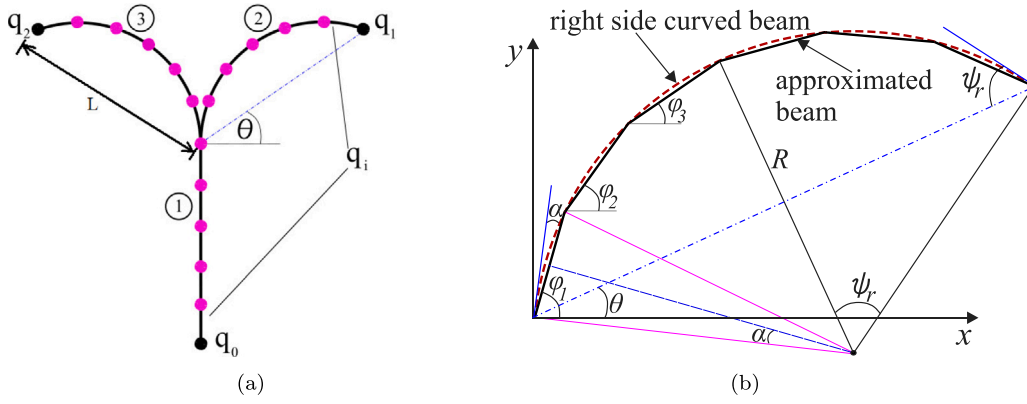


Fig. 2. Figure showing (a) finite element discretization of a unit cell and three constituent beam members numbered as 1 (vertical beam), 2 (right beam) and 3 (left beam), respectively. Each beam is discretized with some finite elements and then assembled to obtain the global matrices. q_0 , q_1 and q_2 denote the boundary degrees of freedom and q_i denotes the internal degrees of freedom and (b) discretization procedure of a single curved beam (right beam) and the geometric details required for doing finite element assembling. The curved beam is approximated by considering a number of straight Timoshenko beams. θ , ψ_r , R , α and ϕ_i are the cell angle, curvature angle of the right beam, radius, curvature angle for a single finite element, and angle between the global and local co-ordinate system for the finite elements, respectively.

where the angle between the local and global axial directions of the beam ϕ depends on the number of finite elements considered to discretize the beam. In Fig. 2 the ϕ corresponding to each finite elements are shown ($\phi_i, i = 1, 2, \dots, n$). Angle ϕ_i can be expressed as the function of the curvature angle ψ of the whole beam, number of finite elements to discretize the curved constituent beam (n) and cell angle θ . The connection angle for the three straight beam unit cell model of a hexagonal lattice is more simple and it is given in [34]. The beam model of some unit cell with one straight and two curved beams approximated by many small Timoshenko beams and connected under different angles according to the local coordinate system are assembled by taking into account matrices from Eq. (9) in the following manner

$$\mathbf{K} = \sum_{e=1}^{n_{ele}} \mathbf{K}_g^e, \quad \mathbf{M} = \sum_{e=1}^{n_{ele}} \mathbf{M}_g^e, \quad (12)$$

where \mathbf{M} and \mathbf{K} are the global mass and stiffness matrices of the unit cell and $n_{ele} = 3 \times n$ (the same number of finite elements are considered for each constituent beam member) is the number of elements in the unit cell. The final equation for the unit cell finite element model is of the form

$$\mathbf{M}\dot{\mathbf{q}} + \mathbf{K}\mathbf{q} = \mathbf{f}. \quad (13)$$

2.4. Dispersion relations for the periodic unit cell

By using the previously described concept, a corresponding eigenvalue problem can be established whose solution gives dispersion curves i.e. frequencies in terms of wavenumbers.

To get the dispersion relations and investigate the band structure of the unit cell we need to utilize the previous finite element model and corresponding periodic boundary condition. Let us first introduce the harmonic solution $\mathbf{q}(x, t) = \mathbf{q}(x)e^{i\omega t}$ into the Eq. (13), which yields

$$(\mathbf{K} - \omega^2 \mathbf{M})\mathbf{q} = \mathbf{0}, \quad (14)$$

where ω is the frequency of the free wave propagation. Here, the force vector \mathbf{f} is neglected and the vector \mathbf{q} of nodal displacements are considered as

$$\mathbf{q} = \{q_0 \quad q_1 \quad q_2 \quad q_i\}^T, \quad (15)$$

with q_0, q_1 , and q_2 denoting the vectors of nodal displacements at unit cell nodes while q_i are degrees of freedom of internal nodes (see Fig. 2 (a)). By employing Bloch's theorem and periodic boundary conditions at the nodes of a unit cell is defined as follows

$$q_1 = e^{k_1} q_0, \quad q_2 = e^{k_2} q_0. \quad (16)$$

where k_1 and k_2 are the wavenumbers as mentioned in Appendix B. By utilizing the Eq. (16) we can apply transformation matrix to the global vector of nodal displacements in the following manner

$$\mathbf{q} = \mathbf{T}_b \mathbf{q}_r, \quad (17)$$

yielding the global vector of nodal displacements in the reduced form $\mathbf{q}_r = \{q_0 \quad q_i\}^T$ while matrix \mathbf{T}_b is given as

$$\mathbf{T}_b = \begin{bmatrix} \mathbf{I} & \mathbf{0} \\ \mathbf{I}e^{k_1} & \mathbf{0} \\ \mathbf{I}e^{k_2} & \mathbf{0} \\ \mathbf{0} & \mathbf{I} \end{bmatrix}. \quad (18)$$

By considering the Eq. (17) into Eq. (14) and pre-multiplying the results with the Hermitian (complex conjugate) transpose matrix \mathbf{T}_b^H results in

$$(\mathbf{K}_r(k_1, k_2) - \omega^2 \mathbf{M}_r(k_1, k_2))\mathbf{q}_r = \mathbf{0}, \quad (19)$$

where the reduced mass and stiffness matrices are of the form

$$\mathbf{M}_r(k_1, k_2) = \mathbf{T}_b^H \mathbf{M} \mathbf{T}_b, \quad (20)$$

$$\mathbf{K}_r(k_1, k_2) = \mathbf{T}_b^H \mathbf{K} \mathbf{T}_b.$$

The eigenvalue problem Eq. (19) can be solved by considering a set of values for k_1 and k_2 in the first Brillouin zone to obtain the dispersion surfaces $\omega = \omega(k_1, k_2)$. The dimension of the eigenvalue problem determines the number of dispersion surfaces. The geometry of the reciprocal lattice depends on the cell angle (θ) of the lattice and the reciprocal lattice vectors ($\mathbf{e}_1^*, \mathbf{e}_2^*$) can be obtained by following the standard procedure mentioned in Appendix A. The author refers [35] for more details on the symmetry and Brillouin zone. The symmetry of the unit cell dictates the symmetry of the Brillouin zone. Considering the symmetry property of the first Brillouin zone the irreducible Brillouin zone (IBZ) can be obtained. Eventually, the computational effort can be substantially reduced by considering the values of wavenumbers varying along the contours of the IBZ. The same IBZ in the reciprocal lattice and its contours for the hexagonal and re-entrant lattices as given in [20,34] are used and shown Table 1.

3. Numerical study and discussion

The dispersion characteristics of the new set of curved hexagonal lattices (see Fig. 1) are investigated considering Timoshenko beam-based modelling for the constituent beam members. In this study, hexagonal and re-entrant lattices along with their variant where the curvature of the constituent curved beams are reversed are considered.

Table 1
The boundary points of the irreducible Brillouin zone of hexagonal and re-entrant lattice structures.

Type of periodic structure	Hexagonal structure	Re-entrant structure
	$0^\circ \leq \theta < 90^\circ$	$-30^\circ < \theta \leq 0^\circ$
O	(0, 0)	(0, 0)
A	$2\pi(1/(4 \sin^2 \phi), -1/(4 \sin^2 \phi))$	$2\pi(1/2, -1/2)$
B	$2\pi(1 - 1/(4 \sin^2 \phi), 1/(4 \sin^2 \phi))$	$2\pi(1 - 1/(4 \cos^2 \phi), -1/(4 \cos^2 \phi))$
C	$2\pi(1/2, 1/2)$	$2\pi(1/(4 \cos^2 \phi), 1/(4 \cos^2 \phi))$

These geometries are variants of the conventional hexagonal lattice formed by curved beams. Thus, unlike the conventional case with the cell angle, θ another geometric parameter, curvature angle ψ is appeared in our investigation. The main motivation of this work is to exploit ψ to enhance the band-gap characteristics without including local resonators. A study on the band-gap analysis considering the prestressed beam with embedded masses shows additional band-gaps for the hexagonal lattice [34] mostly in the mid or high-frequency region. The present work demonstrates the exploitation of the curved beams to obtain both low and high-frequency band-gaps along with their widening. All the codes for the numerical calculation are developed in MATLAB. The band-gaps with very thin widths are neglected for all the figures.

The dispersion analysis is performed considering the wave vector (\mathbf{k}) varying along the contour $O - A - B - C - O$ (see Fig. A.1). The material and geometric parameters considered for the analysis are taken from [34] for the sake of validation and they are used for the present analysis as well. The properties are as follows: elastic modulus $E = 210 \times 10^9$ Pa, mass density $\rho = 25 \times 10^3$ kg/m³, Poisson's ratio $\nu = 0.25$, slenderness ratio $\beta = t/L = 1/15$, length of the beam $L = 0.125$ m (see Fig. 2). Frequencies (ω) obtained from the eigenvalue analysis to get the dispersion diagrams are normalized with the first flexural natural frequency of the simply-supported beam to maintain consistency with the previous literature. The first flexural natural frequency can be expressed as $\omega_0 = \pi^2/L^2 \sqrt{EI/\rho A}$ and the expression for the normalized frequency becomes $\Omega = \omega/\omega_0$. The second moment of inertia is denoted as $I = bt^3/12$ and the area $A = bt$ (b and t are the widths and the thickness of the beam, respectively). The coupled effect of cell angle and curvature angle is discussed in the following sections.

3.1. Converge study and validation of band structures

Here we perform a convergence study to adopt the number of necessary finite elements required in curved beam discretization to achieve satisfying accuracy. For this, a free vibration analysis of the unit cell considering both pinned–pinned and clamped–clamped boundary conditions is performed. Both boundary conditions are applied to all boundary nodes of the unit cell given in Fig. 2(a). The natural frequencies for the first few modes are obtained by increasing the overall number of elements in a unit cell for $\theta = 30^\circ$ and $\psi = 50^\circ$. Table 2 shows that 30 finite elements per beam in a unit cell (90 in the whole unit cell) gives satisfying accuracy that is used in the rest of our analysis.

Here, the band structure and the corresponding dispersion surfaces obtained for two cases, 1. curved hexagonal lattice with $\theta = 30^\circ$ and $\psi = 30^\circ$, and 2 are shown. Curved hexagonal lattice with $\theta = 30^\circ$ and reverse $\psi = 30^\circ$. Fig. 3(a) and Fig. 3(b) verify that the band structure of the curved hexagonal lattice and corresponding band-gaps in the irreducible Brillouin zone are matching with the 3D dispersion surface plots for the whole Brillouin zone. Fig. 3(c) and Fig. 3(d) are showing the same thing for the re-entrant hexagonal lattice.

The main observation for both cases is that the band structures display the emergence of new band-gaps in different frequency regions compare to the hexagonal/re-entrant lattices with straight beam elements. The details of the influence of curvature angle and also the coupled effect of θ and ψ are discussed in the next sections.

Table 2
Convergence study for the number of finite elements used to discretize the constituent beam members in the unit cell. The natural frequencies are normalized by $\omega_0 = \pi^2/L^2 \sqrt{EI/\rho A}$.

Natural frequencies	Pinned–pinned Number of elements			Clamped–clamped Number of elements		
	10	20	30	10	20	30
ω_1	0.4408	0.4539	0.4585	0.8547	0.8705	0.8761
ω_2	1.3340	1.3331	1.3328	1.9149	1.9154	1.9154
ω_3	2.8290	2.8224	2.8226	3.5826	3.5760	3.5757
ω_4	3.1224	3.1210	3.1223	3.8779	3.8774	3.8788
ω_5	4.4554	4.4580	4.4583	5.5123	5.5156	5.5160
ω_6	5.7033	5.7472	5.7667	6.0355	6.0856	6.0969
ω_7	6.5544	6.3622	6.2988	6.6288	6.4559	6.4088
ω_8	6.7244	6.6902	6.6874	7.6393	7.6283	7.6307
ω_9	8.8636	8.8690	8.8693	9.6770	9.6541	9.6474
ω_{10}	9.4202	9.4725	9.4928	10.4968	10.4798	10.4825

3.2. Finite element validation of band-gap characteristics with finite lattice

In this section, finite element verification of the band structure is performed considering a finite lattice. The lattice has 20 cells in the x -direction and 9 cells in the y -direction. The unit cell of the lattice structure has the same geometric and material properties as mentioned before with $\theta = 30^\circ$ and $\psi_l = \psi_r = 30^\circ$. The left boundary of the lattice is fixed and the excitation is applied on the other side as shown in Fig. 4. We consider three different locations to measure the responses. The geometry and the meshing are performed in Gmsh and the finite element analysis with the postprocessing performed in MATLAB. Each beam of the corresponding unit cell is discretized with 10 finite elements which result in 5850 elements in total for the whole structure.

The transmittance for the finite lattice is obtained to verify the results obtained from the periodic analysis of the unit cell. The steady-state frequency responses are obtained followed by the transmittance at various measuring points. The excitation is applied on the x -direction and only the transmittance plot for the measuring point 3 is shown for the sake of brevity in the Fig. 5(a). The expression for the transmittance is as follows:

$$U_i = 20 \log \frac{U_m}{U_e} \quad (21)$$

where U_m and U_e are the displacements of the measuring and excitation points, respectively. The band-gap characteristics is also shown in Fig. 5(b) for comparison. It is observed from the analysis that the reduction in transmittance is more for the measuring points which are located far from the excitation point. We can see that there is a reduction in the transmittance in frequency ranges corresponding to the band gap frequencies. The frequency ranges for the first three band gaps are matching quite well with the frequency ranges of the transmittance peaks. However, the band gap position near frequency 8 is deviating from the frequency range of the transmittance peak. The reason behind this is due to the finite number of unit cells in the lattice and also the discretization of the finite element model might not be enough to capture the high frequency region. This investigation verifies the band gap analysis considering the unit cell.

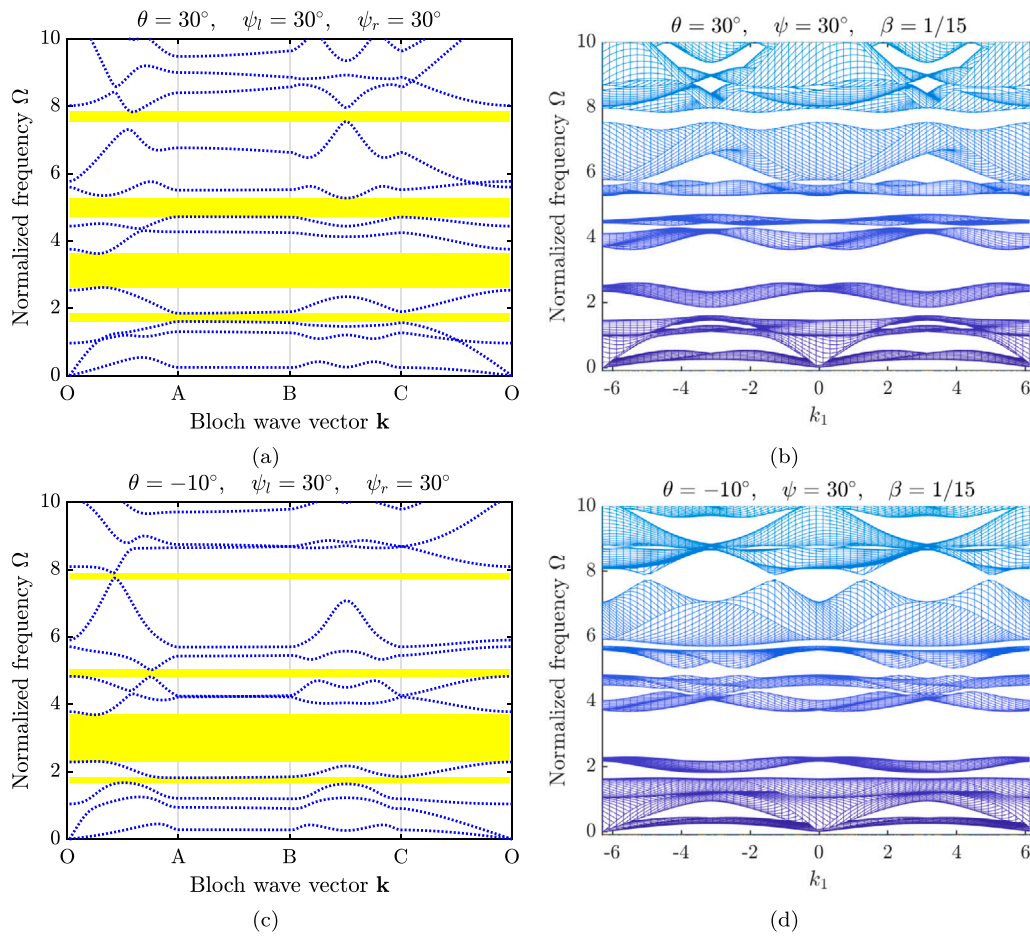


Fig. 3. Frequency band structures for (a) the curved hexagonal lattice with $\theta = 30^\circ$ and $\psi_l = \psi_r = 30^\circ$, (b) dispersion surface of curved hexagonal lattice with $\theta = 30^\circ$ and $\psi_l = \psi_r = 30^\circ$, (c) the re-entrant curved hexagonal lattice with $\theta = -10^\circ$ and $\psi_l = \psi_r = 30^\circ$ for constitutive curved beam, (d) dispersion surface of re-entrant curved hexagonal lattice with $\theta = -10^\circ$ and $\psi_l = \psi_r = 30^\circ$ constitutive curved beam. θ , and ψ are cell angle and curvature angle, respectively.

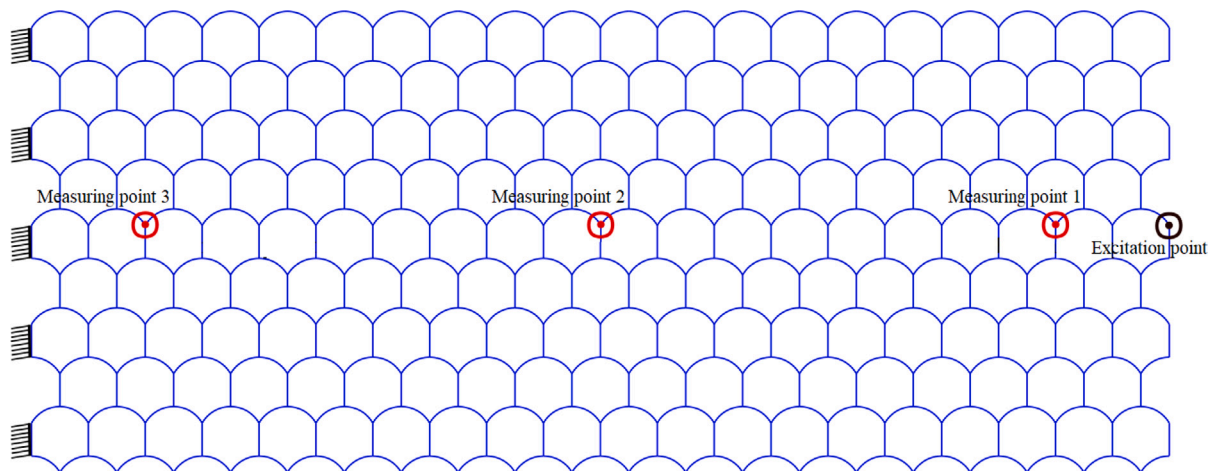


Fig. 4. The geometry of finite lattice with boundary condition along with the excitation and measuring points.

Next, the time response for the excitation and measuring points are also obtained. The lattice was subjected to loading at the excitation point with a modulated pulse with two different frequency content shown in Fig. 6. Fig. 6(a) shows the tone burst signal with frequency content around 140 Hz ($\Omega = 0.2$; long wavelength region) and Fig. 6(b) shows the same with frequency content 2100 Hz ($\Omega = 3$; lies inside the

band gap). The time history of the different measuring points along with the excitation point are shown in Figs. 7 and 8 for two different modulated pulse loadings mentioned in Fig. 6. It is observed in Fig. 7 the amplitudes of the responses are of the same order. The amplitude of responses for the measuring points does not follow any trend; i.e the amplitude of the response of measuring point 3 is higher than

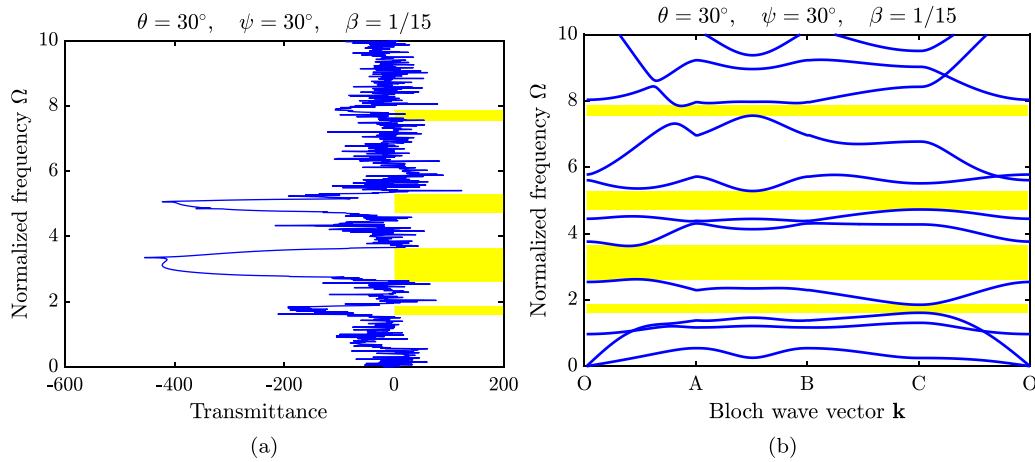


Fig. 5. Figure showing (a) transmittance and the (b) frequency band structures of the corresponding unit cell with $\theta = 30^\circ$, and $\psi_l = \psi_r = 30^\circ$.

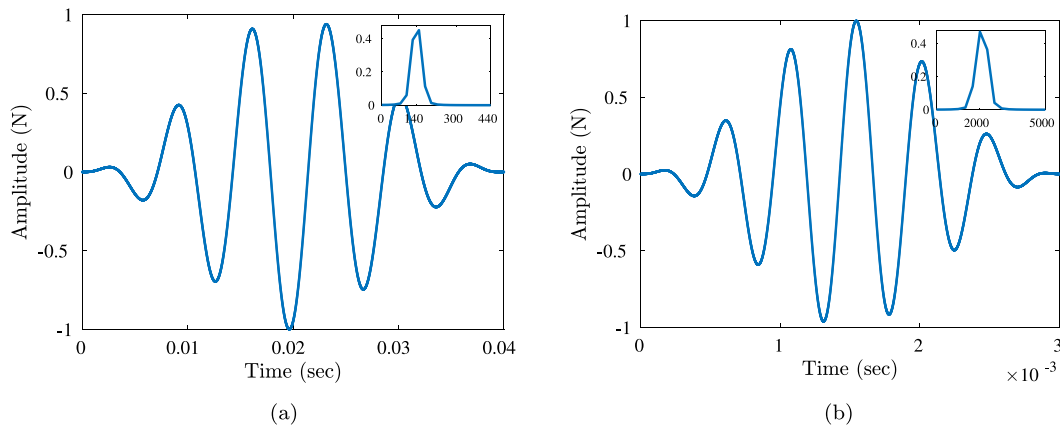


Fig. 6. Figure showing tone burst signals with a frequency content of around (a) 140 Hz (normalized $\Omega = 0.2$) and (b) 2100 Hz (normalized $\Omega = 3.0$).

measuring point 2. Whereas, for Fig. 8 the amplitude reduces gradually as one goes far from the excitation point. This is because the frequency content lies within the band gap region, unlike in the previous case.

3.3. Curved hexagonal lattice

The effect of the curvature angle on the dispersion characteristics of the hexagonal and re-entrant lattices with constituent curved beams is investigated through the Bloch wave analysis. Incorporation of the curved beam as the constituent beam originates new band-gaps and also induces band-gap widening.

The influence of the curvature angle can be observed in Fig. 9. In this plot the hexagonal straight (see Fig. 9(a)) and curved hexagonal lattices (Fig. 9(b) – Fig. 9(d)) is considered. The cell angle θ is kept constant at 30° and the ψ is varied.

Comparing Fig. 9(a) and Fig. 9(b) one can observe that unlike the conventional hexagonal lattice with straight constituent beam there is a new band-gap opening near $\Omega = 3$ and the width of the former band-gap for $4 \leq \Omega \leq 6$ is slightly reduced. New band-gaps are continuously emerging as soon as the ψ is increasing. Fig. 9(c) shows four band-gaps for the case of $\psi_{l,r} = 30^\circ$ located in both lower and higher frequency regions. To have a more clear picture of the influence of curvature angle on the evolution of band-gaps Fig. 9(d) is obtained by varying ψ and keeping $\theta = 30^\circ$. For low values of curvature angle, there is only one gap that is equivalent to the case of hexagonal lattice when $\theta = 30^\circ$. At a certain value of ψ close to 5° the second band-gap appears. A further

change of the curvature angle yields more band-gaps and five of them in total exists for $\psi = 50^\circ$. The width of band-gaps also varies with some of them slightly shifting towards lower frequency regions.

One interesting feature that can be observed in band structures of hexagonal lattices with straight constituent beams is the veering and locking of frequency bands. These phenomena that appear when corresponding dispersion branches mutually interact are well known in weakly coupled mechanical systems [36,37]. Veering and/or locking were observed by different authors for a variety of planar lattice topologies such as hexagonal, trigonal and square honeycomb lattices [38], hierarchical lattices [27] or frame grid lattices with resonators [39]. Veering can be viewed as a localized zone in the dispersion diagram that appears between the pairs of eigenmodes, where eigenvalues do not cross but veer away. In the case of locking, the merging of two non-zero eigenfrequencies occurs to form a complex-conjugate pair (e.g. see [37]). Observing Fig. 9(a) for the conventional hexagonal lattice one can notice three characteristic veering and locking points that appear between the third and the fourth as well as eighth and tenth dispersion branches. As earlier described in [39], two closely spaced modes are having identical mode shapes which means that a small change in energy can shift the system from one mode to another in the veering zone. However, introducing the curved beam-based configuration of hexagonal lattices yields much different behaviour of band structure with fewer veering points. An increase of curvature angle causes some new band-gaps to open at the frequency of veering and/or locking points along with the obvious detachment of dispersion

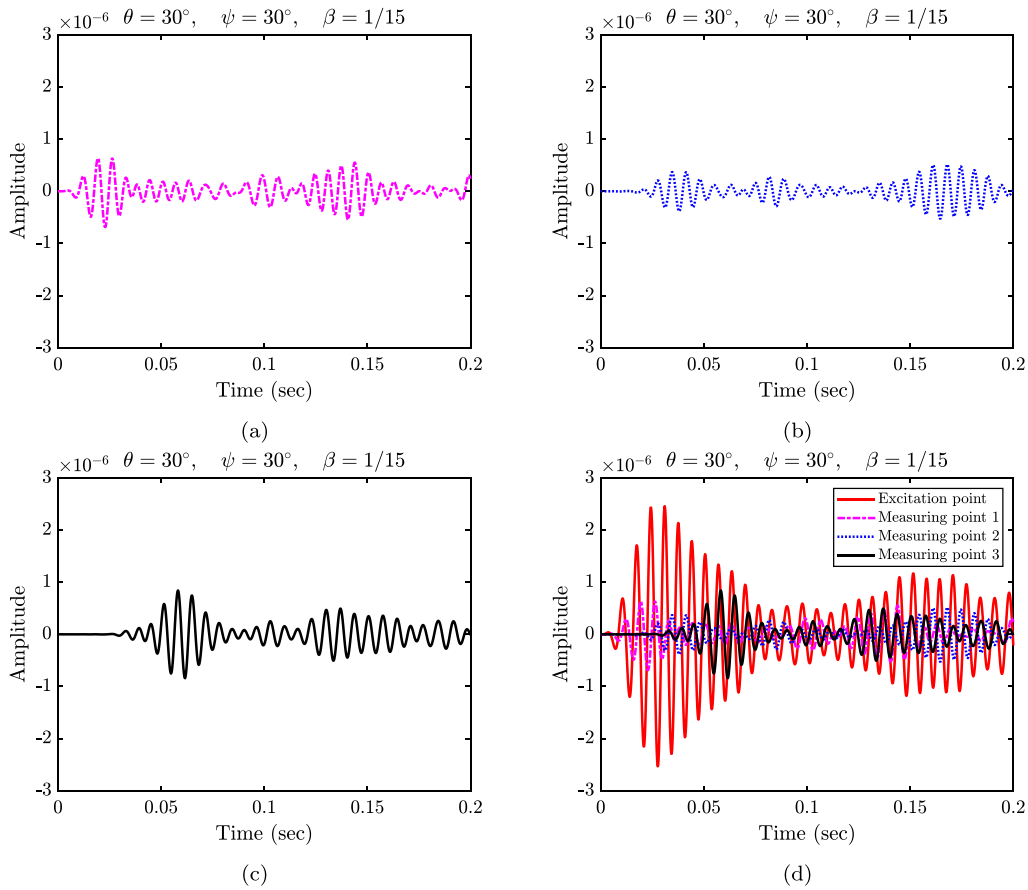


Fig. 7. Time response of three measuring points on the curved hexagonal finite lattice with $\theta = 30^\circ$ and $\psi_l = \psi_r = 30^\circ$ subjected to harmonic excitation of around 140 Hz (normalized $\Omega = 0.2$) applied on the global x direction at the excitation point (shown in Fig. 4) (a) response at measuring point 1, (b) response at measuring point 2, (c) response at the measuring point 3, and (d) response of all points.

branches. Therefore, the energy levels of such separated modes are much higher and jump-up or jump-down phenomena are difficult to occur in such systems. Similar behaviour can be noticed in different curvature beam configurations and both modified hexagonal and re-entrant lattices. According to [37], effects analogous to locking are common in stability analysis where for example some instabilities can be predicted in certain hydrodynamic systems. Having in mind that many veering and locking points vanish in modified hexagonal and re-entrant lattices, it can be also concluded that wave modes become more stable after introducing the curved beam-based configuration. It is also evident from the Fig. 9 that the group velocities which is the slope of the dispersion curves ($c_g = \partial\Omega/\partial\mathbf{k}$) for the longitudinal waves at long wavelength limits reduce with increase in ψ .

Another interesting curved lattice configuration, when one of the curvature angles ψ is reversed (see Fig. 1(b)) is also studied. The reversed curvature configuration is depicted as positive and negative ψ values for the two constitutive beam elements. The curvature angles for the left and right curved beams are denoted as ψ_l and ψ_r , respectively. The band structure of these two cases is much different compared to the case with both positive curvatures. Fig. 10 is showing the band structures of the curved hexagonal lattice for beam members with reverse curvature. In this plot, Fig. 10(a) shows the dispersion diagram with very small ψ values for both curved beam members which shows a very good match with the conventional hexagonal lattice. In the following figures (Fig. 10(b) – Fig. 10(c)) the curvature angle is increased and it shows occurrence and disappearance of band-gaps. The nature of the dispersion diagrams is different from the previous case where both curvature angles were positive. Overall, the number of band-gaps is less in this case as well as the widening of the band-gaps. Comparing Figs. 9(d) and 10(d) it is observed that even for $\psi = 50^\circ$ the

number of band-gaps are less for lattice considering curved beam with reverse curvature. The band-gap which appeared near $\Omega = 5$ eventually gets narrower and again widens at ψ close to 42° . Also, the width of the band-gap which occurs near $\Omega = 3$, increases with ψ like in the previous case but decreases with increasing ψ after ψ around 25° . Although the nature of the band-gap shifting towards the lower frequency range is similar to the previous case.

3.4. Curved re-entrant lattice

The same analysis is also performed for the re-entrant case with a positive curvature angle for both of the constituent beam members and with reverse curvature. The influence of the curvature angle is observed in Fig. 11.

In this analysis, the cell angle for the re-entrant lattice is considered as 10° . The dispersion diagram for the re-entrant lattice with the straight beams is shown in Fig. 11(a). The value of the curvature angles is then increased eventually to investigate the effect of the curvature angle on the dispersion relationship for the re-entrant lattice. Plots Fig. 11(b) – Fig. 11(d) show the details of the study. Comparing Fig. 11(a) and Fig. 11(b) it is observed that unlike the conventional re-entrant lattice with straight constituent beam there are two a new band-gap opening near $\Omega = 8$ and 3. As the value of $\psi_{l,r}$ is increased to 30° the width of the band-gap near $\Omega = 3$ increases and two new band-gaps appear near $\Omega = 5$ and 2. To have a more clear picture of the influence of curvature angle, the evolution of band-gaps with ψ is obtained and shown in Fig. 11(d) while keeping $\theta = 30^\circ$. One can observe that the width of the band-gap which appeared near $\Omega = 3$ keeps increasing up to curvature angle 22° and then remains almost

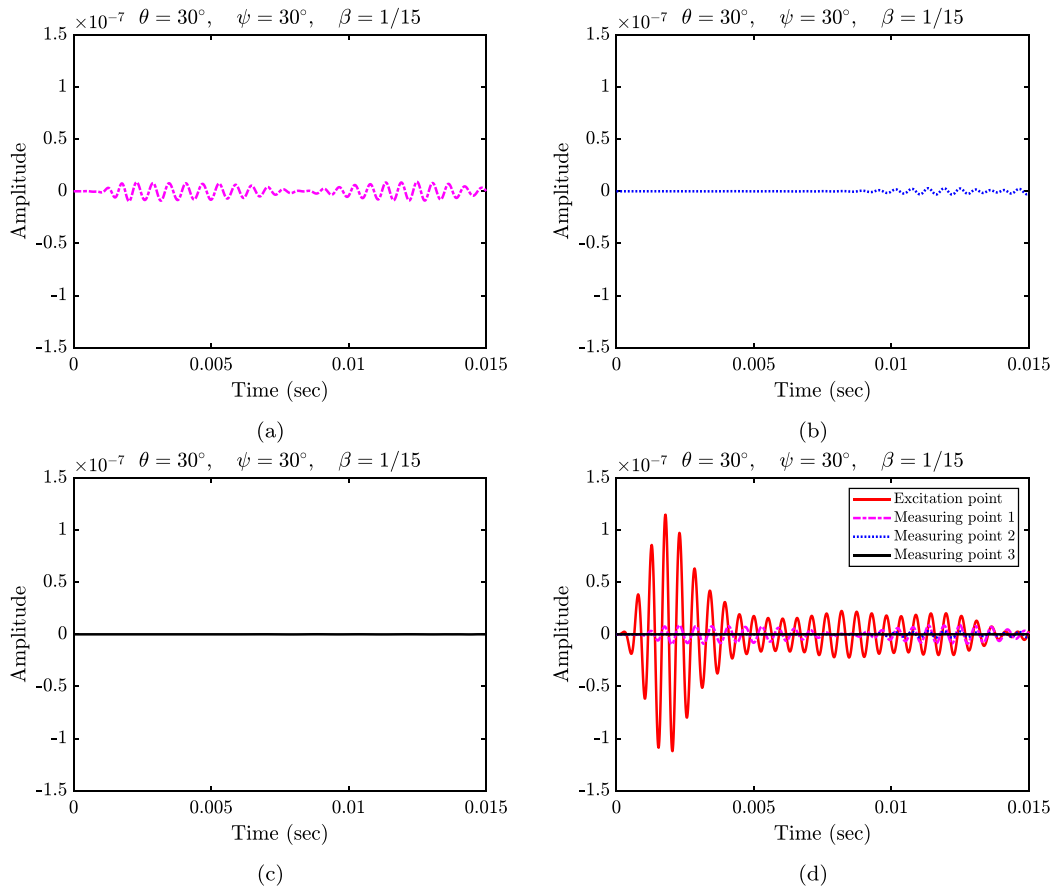


Fig. 8. Time response of three measuring points on the curved hexagonal finite lattice with $\theta = 30^\circ$ and $\psi_l = \psi_r = 30^\circ$ subjected to harmonic excitation of around 2100 Hz (normalized $\Omega = 3.0$) applied on the global x direction at the excitation point (shown in Fig. 4) (a) response at measuring point 1, (b) response at measuring point 2, (c) response at the measuring point 3, and (d) response of all points.

unaltered for the rest. Though the band-gap shifts towards the lower frequency ranges. The shifting of band-gaps to the lower frequency range is true for other band-gaps as well. With increasing ψ the band-gap which appeared near $\Omega = 3$ disappears around $\psi = 35^\circ$ and regenerates again after a while. The width of these band-gaps then keeps increasing with ψ . Another band-gap appears near $\psi_{l,r} = 25^\circ$ and its width keeps increasing towards the lower frequency region. It is noticed that at $\psi_{l,r} = 50^\circ$ there are 5 band-gaps present. A similar investigation is performed for re-entrant lattice with configuration considering both positive and negative ψ for the curved beam in the unit cell (see Fig. 1(b)). This configuration is named a unit cell with a reverse angle. The band structure with reverse curvatures is much different compared to the case with both positive curvatures. Fig. 12 is showing the band structures of the curved re-entrant lattice reverse configuration. Fig. 12(a) shows the dispersion diagram with very small ψ values for both curved beam members which shows a very good match with the conventional hexagonal re-entrant lattice. In the following figures (Fig. 12(b) and Fig. 12(c)) the curvature angle is increased. It shows occurrence of new band-gaps in lower as well as higher frequency regions in the lower as well as higher frequency regions for $\psi_l = 30^\circ, \psi_r = -30^\circ$ (Fig. 12(c)) case.

The nature of the dispersion diagrams is different from the re-entrant case with both positive curvatures. Overall the number of band-gaps is less in this case as well as the widening of the band-gaps. Comparing Figs. 11(d) and 12(d) it is observed that even for $\psi = 50^\circ$ the number of band-gaps are less for lattice considering curved beam with reverse curvature. From Fig. 12(d) one can notice that the width of the band-gap which appeared near $\Omega = 3$ near $\psi = 15^\circ$ increases up to around $\psi = 21^\circ$ and continues for higher values of ψ and the width decreases eventually. The small band-gap which appears near

$\Omega = 5$ increase its width up to $\psi = 26^\circ$ and then decreases until $\psi = 35^\circ$. Again the band-gap starts to grow and continues while shifting towards the lower frequency region. The overall nature of the band-gap is shifting towards the lower frequency region with increasing ψ . Unlike the previous case with both positive curvature angles, the number of band-gaps and widths are less for the case with reverse curvature.

3.5. Effect of cell angle on the band-gaps

The effect of the cell angle on the band-gap characteristics is summarized in the Fig. 13. To obtain the effect of θ the ψ value is fixed to 50° for all the cases. The effect of θ on the curved hexagonal lattice is shown in Fig. 13(a). It is observed that for the two lower band-gaps the width remains the same while for the third one the band-gap increase with the θ . For the band-gap in the higher frequency, the width of the band-gap is highest for lower θ values and decreases with increasing θ . There are two band-gaps below $\Omega = 6$ and 7 whose widths increase with θ . Fig. 13(b) shows the effect of θ on the hexagonal lattice with a reverse curvature angle for the constituent beam. It can be observed that the effect of the θ on the width of the band-gap is almost minimal. There is a new band-gap opening in the high-frequency region near $\theta = 25^\circ$. The influence of θ on the curved re-entrant lattice is shown in Fig. 13(c). The width of the band-gaps in the lower frequency region remains unaltered while the width of the mid-frequency one increase with θ . There are some small openings of band-gaps at higher θ values. The width of the band-gap in the higher frequency region decreases with increasing θ . Unlike the previous case with reverse curvature (see Fig. 13(b)) for the re-entrant case with reverse curvature the influence of θ is negligible except the opening of very small band-gaps

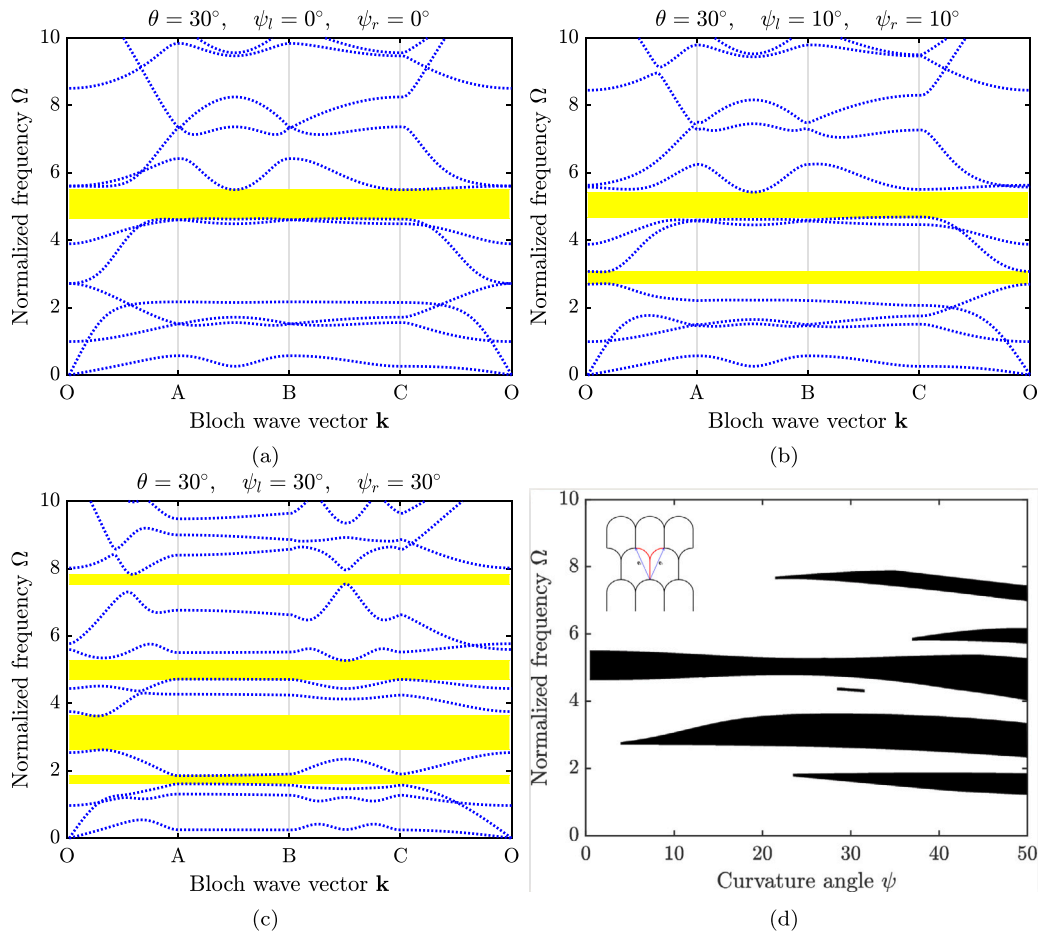


Fig. 9. Figure showing frequency band structures of the (a) hexagonal lattice with straight beam members with $\theta = 30^\circ$, and curved hexagonal lattice with $\theta = 30^\circ$ and (b) $\psi_l = \psi_r = 10^\circ$, (c) $\psi_l = \psi_r = 30^\circ$, and (d) evolution of the frequency band-gaps with curvature angle ψ considering cell angle $\theta = 30^\circ$. θ and ψ are the cell angle and curvature angle, respectively.

for different θ values. It is clear from the plots that the effect of θ for the lattice with the reversely curved beam is very less compared to the other case.

3.6. The iso-frequency contours

Important conclusions regarding the existence of stop bands in lattices are drawn from the band structure analysis. However, we can get a complete picture of the wave propagation in modified lattices only by investigating their directional behaviour. Figs. 14 and 15 are showing contours of dispersion surfaces corresponding to the first four wave modes of six different lattice types whose main geometrical parameters are given in the beginning of this section. These contours, known in the literature as iso-frequency contours, are revealing the direction of the group velocity which is perpendicular to them. This enables one to disclose the directionality of wave propagation in lattices only by knowing their dispersion characteristics. A well known property of homogeneous materials is that wave propagates equally in all directions resulting in circular iso-frequency curves while in anisotropic mediums such as lattices of different topology these contours can have a variety of shapes. Let us superimpose the first Brillouin zone to the iso-frequency contour plots for each of the given wave modes. The first four panels in Fig. 14 are showing the iso-frequency contours of the hexagonal lattice with straight beams. The next four panels are referring to the modified lattice when both curved beams are defined by the positive angle ψ_l and ψ_r while the last four panels are referring to the positive ψ_l and negative ψ_r .

In the first mode of the convectional hexagonal lattice, one can identify six-lobed contour curves that are displaying anisotropic behaviour at certain frequency values. Moreover, a moderate number of iso-frequency contours can be observed in this mode for both lower and higher frequency values, which means that there are no abrupt changes in the corresponding dispersion surface. The second and third modes are displaying different behaviour, where a high number of contours can be seen for low values of frequency and wavenumber while their density is becoming low towards the edges of the Brillouin zone that is attributed to almost flat dispersion surfaces at higher frequencies. In the last wave mode, there are no contours at the boundaries of the Brillouin zone and dispersion surfaces are flat in that region. Elliptical or nearly circular shapes of iso-frequency curves in the last three modes are implying the quasi-isotropic behaviour which suggests an identical speed of wave propagation in all directions mostly associated with the low frequency.

By comparing the iso-frequency surface plots between the conventional and modified curved lattice it is noticed that the same topology of iso-frequency curves is kept in the first mode while there is a significant difference in higher frequency wave modes. For the second wave mode, this change reflects in a slower change of dispersion surfaces for low frequency values due to less density of iso-frequency curves associated with quasi-isotropic behaviour. Towards the boundaries of the Brillouin zone, a lesser number of lobed contours appears due to the flattened dispersion surfaces. The iso-frequency contours drastically change in the third and fourth modes compared to the conventional lattice, where anisotropic behaviour becomes more apparent. This drastic change is

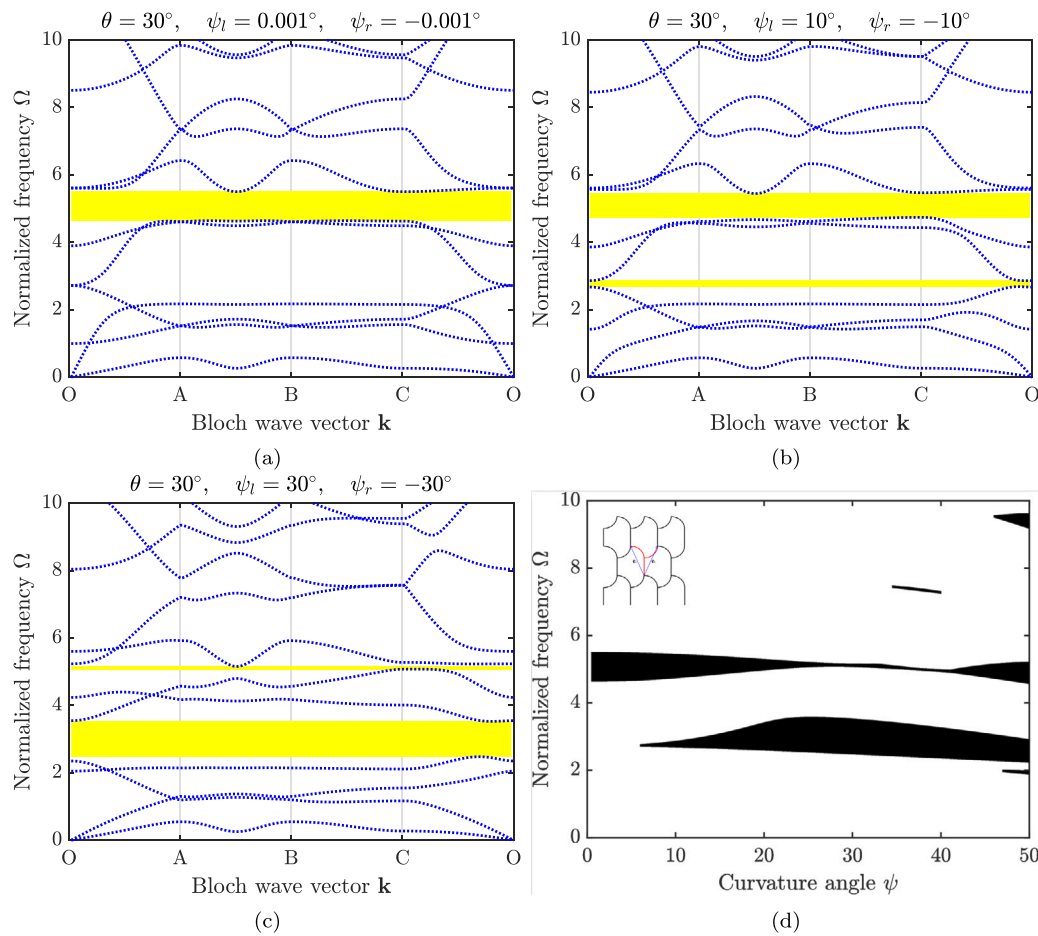


Fig. 10. Figure showing frequency band structures of the curved hexagonal lattice with $\theta = 30^\circ$ and reverse curvature angle for the curved beams (a) $\psi_l = 0.001^\circ$, $\psi_r = -0.001^\circ$, (b) $\psi_l = 10^\circ$, $\psi_r = -10^\circ$, (c) $\psi_l = 30^\circ$, $\psi_r = -30^\circ$, and (d) evolution of the frequency band-gaps with reverse curvature angle ψ considering cell angle $\theta = 30^\circ$. θ and ψ are the cell angle and curvature angle, respectively.

attributed to the fact that in between these bands a new band-gap opens. That causes shifting of the bands to either lower or higher frequencies and their flattening at the edges of band-gaps as well as the reverse appearance of contours associated with the lowest and highest frequency. Similar behaviour can be observed for the lattice with reverse curvatures where in the first mode only smoothed lobed contours can be noticed and slight shifting of the frequency to lower values. The lesser density of contours is present for the lower frequency values indicating the slower change of dispersion surfaces. Again third and fourth modes are displaying much different iso-frequency contours. The directional behaviour of the third mode is more emphasized than the one of the conventional lattice with equally distributed contours indicating the slower change of the dispersion surface within the first Brillouin zone. The fourth band is associated with the band-gap between the fourth and fifth (not given here) band and only fewer contours can be seen due to the flat nature of the corresponding dispersion surface. An interesting wave propagation nature of re-entrant hexagonal lattices was revealed in many previous works. Here, modified re-entrant hexagonal lattices with curved beams are observed and the directional wave propagation behaviour based on iso-frequency contours of the dispersion surfaces of four wave modes is studied. Similar to the previous case, in Fig. 14 the first four panels are referring to the conventional re-entrant lattice, the next four are representing the configuration with both positive curvature angles and the last four are referring to the case with one positive and one negative curvature. Highly directional behaviour of all propagating wave modes can be observed in the conventional re-entrant hexagonal lattice. However, this feature is changed at a certain

amount in the modified lattices. This change is not that pronounced in the first mode like in the other three higher wave modes. Moreover, the high density of low frequency contours in the second and third modes of the conventional lattice is lost in the modified lattice configuration indicating the slower change of dispersion surfaces. In these cases, the contours are evolving from nearly circular to oval shapes thus changing their nature from isotropic to anisotropic one. However, this change is much more smooth in the case of curved beam lattices compared to the conventional one. The main characteristic of the fourth mode iso-frequency contours of the modified lattices is the change from highly directional (conventional case) to almost quasi-isotropic nature of the propagating waves. These wave modes are associated with the emerging band-gap, which causes flattening of dispersion surface at its edges and lower density of iso-frequency contours. As given in [39], square lattice can exhibit sensational wave propagation and anisotropic characteristics due to the negative refraction in lattices having the concave nature of iso-frequency curves. As mentioned previously, circular iso-frequency contours are related to the isotropic nature of propagating waves. However, exotic phenomena such as self-collimation and lensing can be identified from the corresponding concave shapes of iso-frequency contours. More precisely, the self-collimation phenomenon (wave beaming) is associated with the straight edges of the iso-frequency contours with waves propagating in the perpendicular direction to the contours. In the case of lensing, if the iso-frequency contours are converging normal to the contour then the waves having a wavelength within the concave contour are converging and focusing. The concave shapes of iso-frequency curves

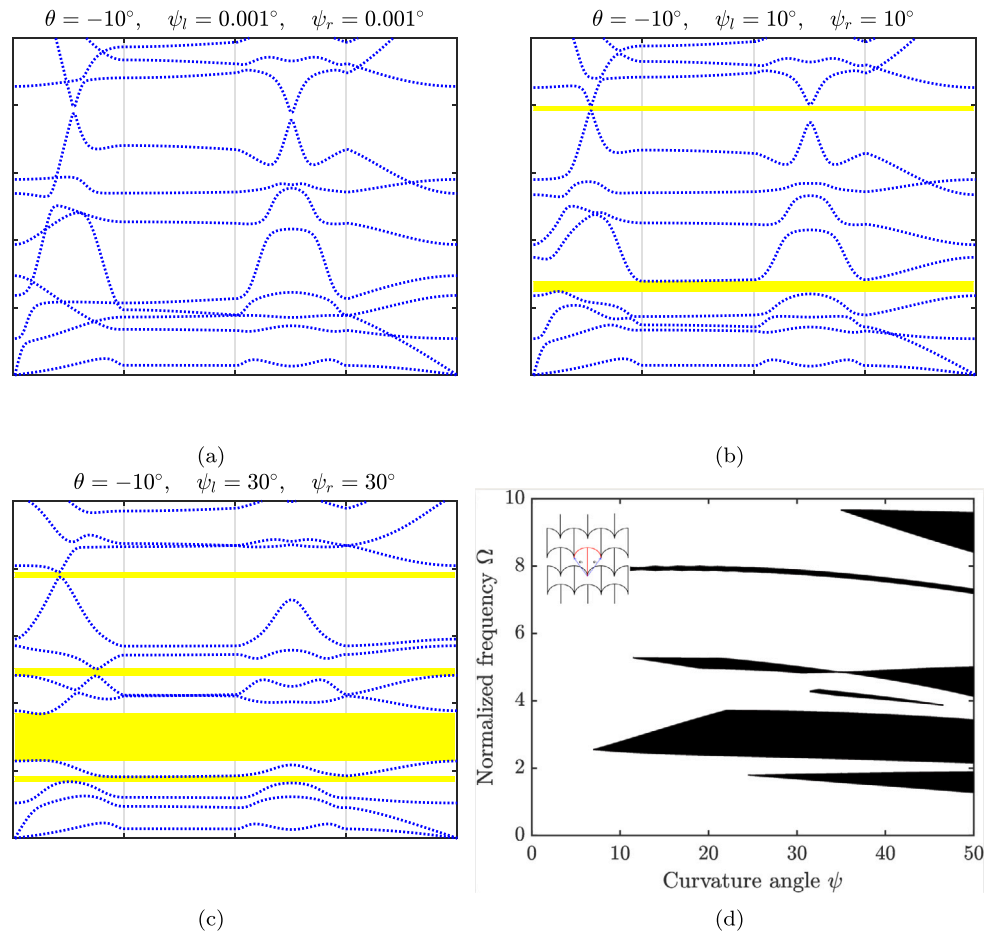


Fig. 11. Figure showing frequency band structures of the (a) re-entrant lattice with straight beam members with $\theta = -10^\circ$, and curved re-entrant lattice with $\theta = -10^\circ$ and (b) $\psi_l = \psi_r = 10^\circ$, (c) $\psi_l = \psi_r = 30^\circ$, and (d) evolution of the frequency band-gaps with curvature angle ψ considering cell angle $\theta = -10^\circ$. θ , and ψ are the cell angle and curvature angle, respectively.

can be observed in both modified hexagonal and re-entrant lattices with curved beam unit cells. These characteristic concave shapes of iso-frequency contour edges can be observed from the last three modes in Fig. 14 as well as in the first and fourth modes in Fig. 15. Moreover, the frequency-dependent directional behaviour of these types of lattices can be also visualized through a polar plot [5], however, this type of analysis is out of the scope of this study.

4. Summary and conclusions

This work focuses on the investigation of the wave propagation characteristics of a class of 2D hexagonal lattice material considering curved beams as constituent beam members. The effect of the geometric parameters of the unit cell is explored for the dispersion properties of those particular lattice materials. Below are the key findings from this present study are as follows.

- The curvature angle of the curved beam plays an important role in the generation of new band-gaps, especially in the lower frequency region. The number of the new band-gaps increases with increasing curvature angle for the lattice with both positive curvature angles. Also, the width of the band-gaps increases for most of the gaps. This is true for the re-entrant case also.
- The position of the veering and locking in the conventional hexagonal lattice indicates the opening zones of the band-gaps for the lattice with curved beams. The number of veering and locking zones gets lesser with the increase in the curvature angle values and the modes become separate from each other.

- Curvature angle has an influence on group velocities for the longitudinal wave mode. With the increase in curvature angle, the values attain lower values as the slope of the dispersion curves gets reduced.
- Unlike the lattice with a positive curvature angle for both beams, the lattice with reverse curvature has not had very promising dispersion characteristics regarding the occurrence of band-gaps. Though there are some band-gaps in the lower frequency.
- The findings from the present investigations show that this class of lattice can be utilized for low-frequency vibration suppression depending on the design requirements.
- Iso-frequency contours revealed a slower change of dispersion surfaces in curved lattices, which is reflected in lesser density of contours and flattening of dispersion curves towards the edges of the first Brillouin zone. At certain frequencies in k -space the contours are displaying both quasi-isotropic and anisotropic behaviour of propagating waves. Moreover, the near circle shapes are indicating quasi-isotropic behaviour while concave shapes and straight edges are referring to the occurrence of phenomena such as lensing and wave beaming.

These promising results could be useful for future guidelines of the hexagonal metamaterials and also serve as benchmark results for further investigation in this domain. Future investigation will focus on the wave propagation characteristics of curved hexagonal lattices coupled with multi-physics along with experimental validation.

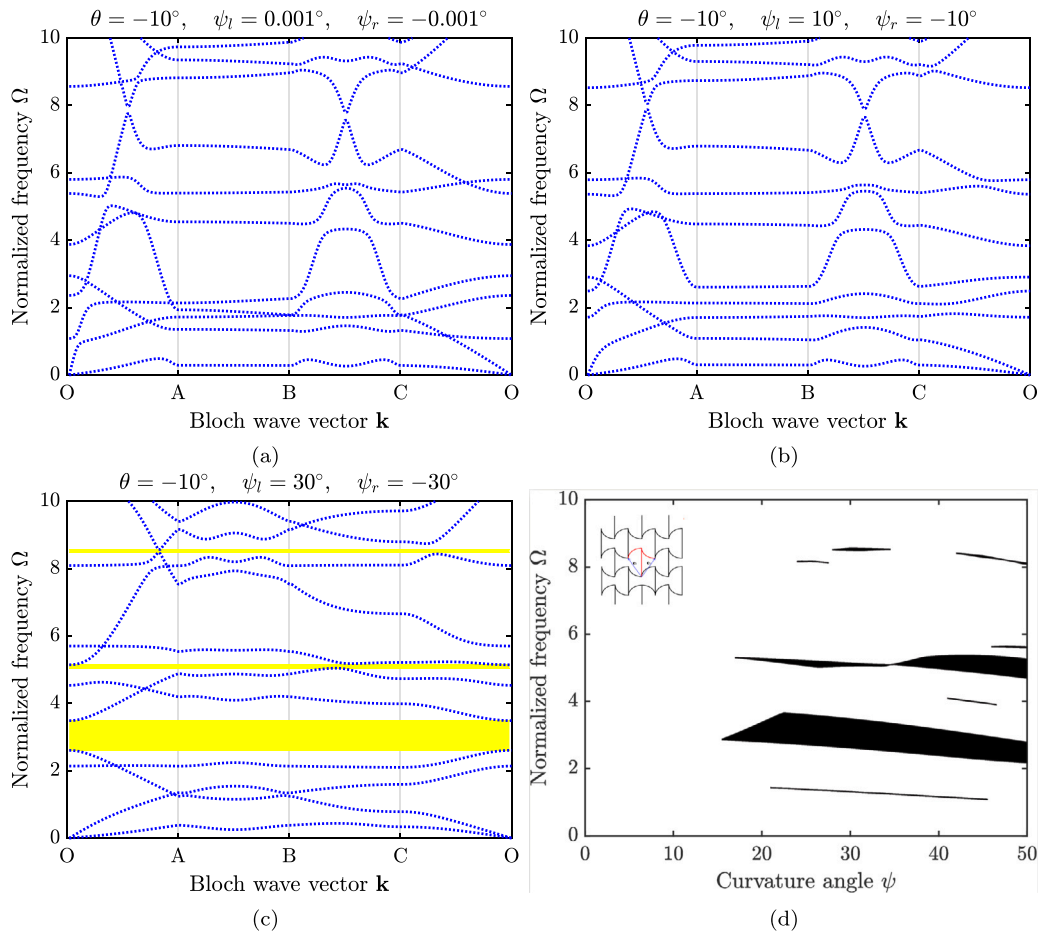


Fig. 12. Figure showing frequency band structures of the curved re-entrant lattice with $\theta = -10^\circ$ and reverse curvature angle for the curved beams (a) $\psi_l = 0.001^\circ$, $\psi_r = -0.001^\circ$, (b) $\psi_l = 10^\circ$, $\psi_r = -10^\circ$, (c) $\psi_l = 30^\circ$, $\psi_r = -30^\circ$, and (d) evolution of the frequency band-gaps with reverse curvature angle ψ considering cell angle $\theta = -10^\circ$. θ and ψ are the cell angle and curvature angle, respectively.

CRedit authorship contribution statement

Shuvajit Mukherjee: Conceptualization, Methodology, Software, Visualization, Writing – original draft. **Milan Cajić:** Visualization, Literature review, Writing – original draft. **Danilo Karličić:** Software. **Sondipon Adhikari:** Project administration, Writing – review & editing.

Declaration of competing interest

The authors declare that they have no known competing financial interests or personal relationships that could have appeared to influence the work reported in this paper.

Data availability

No data was used for the research described in the article.

Acknowledgements

MC and SA acknowledges funding from European Union's Horizon 2020 research and innovation programme under the Marie Skłodowska-Curie grant agreement No. 896942 (METASINK). DK was sponsored by the Serbian Ministry of Education, Science and Technological Development and Mathematical Institute of the Serbian Academy of Sciences and Arts.

Appendix A. Reciprocal lattice vectors

In the case of the unit cell of a hexagonal lattice structure having the positive internal angle θ the basis vectors ($\mathbf{e}_1, \mathbf{e}_2$) are defined in local Cartesian coordinates with unit vectors ($\mathbf{i}_1, \mathbf{i}_2$) as

$$\mathbf{e}_1 = (L \cos \theta, L(1 + \sin \theta))^T, \quad (\text{A.1})$$

$$\mathbf{e}_2 = (-L \cos \theta, L(1 + \sin \theta))^T.$$

Here, L denotes the length of the individual constituent beam and θ is the cell angle. It is well known that in the periodic structure, lattice points with the corresponding base vectors ($\mathbf{e}_1, \mathbf{e}_2$) defines the direct lattice space. Here, for the modified hexagonal lattice with curved beam the lattice points are same as for the conventional one. Therefore, the reciprocal lattice space can be defined in the same manner as in [34] and based on the following relation

$$\mathbf{e}_i \cdot \mathbf{e}_j^* = 2\pi \delta_{ij}, \quad (\text{A.2})$$

with \mathbf{e}_j^* representing the basis vector of the reciprocal lattice and δ_{ij} denoting the Kronecker delta. In that case, the reciprocal lattice vectors of the hexagonal lattice are given as

$$\mathbf{e}_1^* = \left(\frac{1}{2L \cos \theta}, \frac{1}{2L(1 + \sin \theta)} \right)^T, \quad (\text{A.3})$$

$$\mathbf{e}_2^* = \left(-\frac{1}{2L \cos \theta}, \frac{1}{2L(1 + \sin \theta)} \right)^T.$$

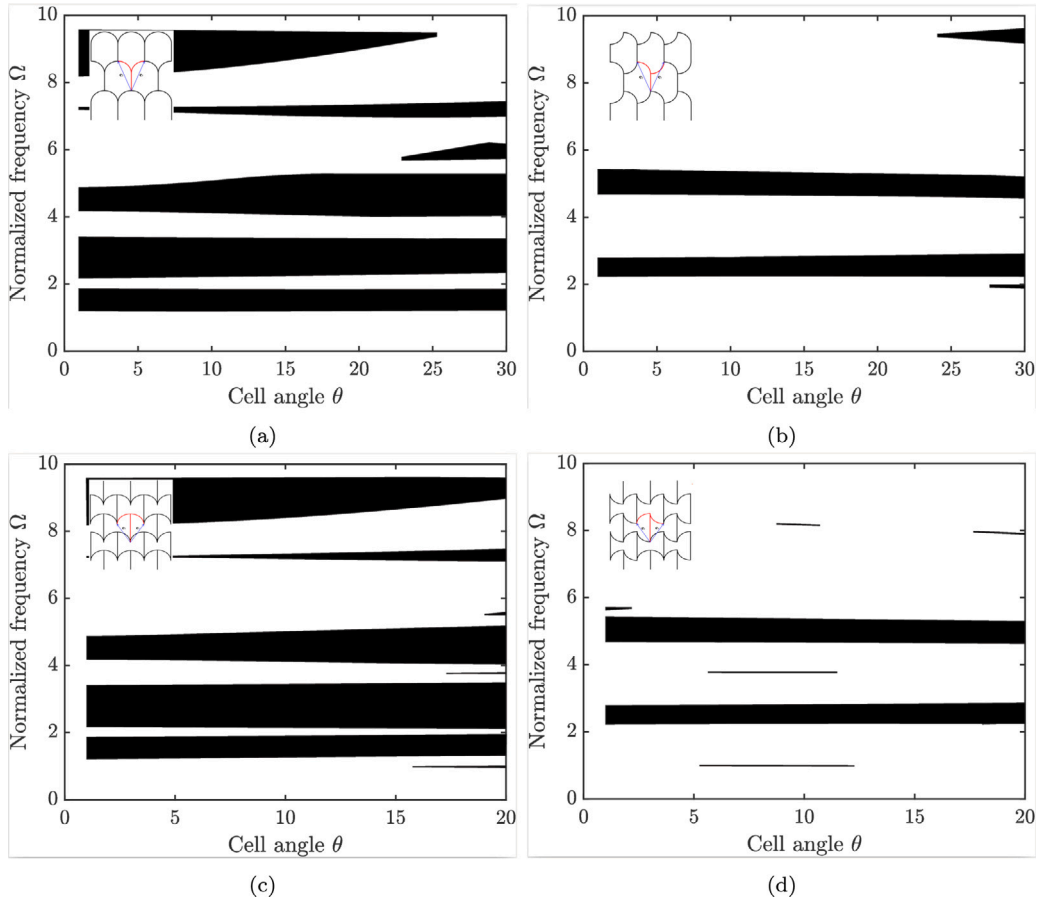


Fig. 13. Evolution of band-gaps with cell angle θ considering $\psi = 50^\circ$ for (a) curved hexagonal lattice, (b) curved hexagonal lattice with reverse curvature, (c) re-entrant curved lattice, and (d) re-entrant curved lattice with reverse curvature. θ , and ψ are the cell angle and curvature, respectively.

Appendix B. Bloch's theorem

The wave propagation characteristics of the curved hexagonal periodic lattice can be obtained by employing the Bloch theorem [34]. Now, if the displacement vector of a point inside the chosen reference unit cell (Fig. 1) corresponding to a wave of frequency ω is $\mathbf{w}(\mathbf{r}_P)$. Then, it can be expressed in the form

$$\mathbf{w}(\mathbf{r}_P) = \mathbf{w}_{P_0} e^{i\omega t - \mathbf{k} \cdot \mathbf{r}_P} \quad (\text{B.1})$$

where \mathbf{w}_{P_0} and \mathbf{k} are the wave amplitude and wave vector, respectively. The position of the point P in the unit cell is denoted by \mathbf{r}_P in the reference cell with respect to $(0,0)$. The position of any point P' in the lattice can be obtained as $\mathbf{r}_{P'} = \mathbf{r}_P + n\mathbf{e}_1 + m\mathbf{e}_2$ where n and m are the integers placed along the direction of the basis vectors \mathbf{e}_1 and \mathbf{e}_2 . According to the Bloch theorem the displacement of the arbitrary point P at (n, m) cell can be expressed as

$$\mathbf{w}(\mathbf{r}_{P'}) = \mathbf{w}(\mathbf{r}_P) e^{\mathbf{k} \cdot (\mathbf{r}_{P'} - \mathbf{r}_P)} = \mathbf{w}(\mathbf{r}_P) e^{\mathbf{k} \cdot (n\mathbf{e}_1 + m\mathbf{e}_2)} = \mathbf{w}(\mathbf{r}_P) e^{nk_1 + mk_2} \quad (\text{B.2})$$

where $k_i = \mathbf{k} \cdot \mathbf{e}_i$ are the wavenumbers ($i = 1, 2$).

Appendix C. The shape function and matrix coefficients

We adopt the same shape functions for the Timoshenko beam element as in [34]:

$$N_1^u(x) = 1 - \xi, \quad N_2^u(x) = 0, \quad N_3^u(x) = 0, \quad (\text{C.1})$$

$$N_4^u(x) = \xi, \quad N_5^u(x) = 0, \quad N_6^u(x) = 0,$$

$$N_1^w(x) = 0, \quad N_2^w(x) = \frac{1 - 3\xi^2 + 2\xi^3 + (1 - \xi)\Phi}{1 + \Phi}, \quad (\text{C.2})$$

$$N_3^w(x) = \frac{h_e(\xi - 2\xi^2 + \xi^3 + \frac{1}{2}(\xi - \xi^2)\Phi)}{1 + \Phi},$$

$$N_4^w(x) = 0, \quad N_5^w(x) = \frac{3\xi^2 - 2\xi^3 + \xi\Phi}{1 + \Phi},$$

$$N_6^w(x) = \frac{h_e(-\xi^2 + \xi^3 - \frac{1}{2}(\xi - \xi^2)\Phi)}{1 + \Phi},$$

$$N_1^\zeta(x) = 0, \quad N_2^\zeta(x) = \frac{6(-\xi + \xi^2)}{h_e(1 + \Phi)}, \quad N_3^\zeta(x) = \frac{1 - 4\xi + 3\xi^2 + (1 - \xi)\Phi}{1 + \Phi}, \quad (\text{C.3})$$

$$N_4^\zeta(x) = 0, \quad N_5^\zeta(x) = \frac{6(\xi - \xi^2)}{h_e(1 + \Phi)}, \quad N_6^\zeta(x) = \frac{-2\xi + 3\xi^2 + \xi\Phi}{1 + \Phi},$$

where $\xi = x/h_e$ denotes the dimensionless axial coordinate and $\Phi = \frac{12EI}{GAk_s h_e^2}$ is the shear deformation parameter.

After adopting these functions, the elements of the stiffness and mass matrix of FE beam model can be written as:

$$K_{ij}^e = \int_0^{h_e} \left[EA \frac{\partial N_i^u}{\partial x} \frac{\partial N_j^u}{\partial x} + EI \frac{\partial N_i^\zeta}{\partial x} \frac{\partial N_j^\zeta}{\partial x} + GAk_s \left(N_i^\zeta - \frac{\partial N_i^w}{\partial x} \right) \left(N_j^\zeta - \frac{\partial N_j^w}{\partial x} \right) \right] dx, \quad (\text{C.4})$$

$$M_{ij}^e = \int_0^{h_e} \left(\rho AN_i^u N_j^u + \rho I N_i^\zeta N_j^\zeta + \rho AN_i^w N_j^w \right) dx, \quad (\text{C.5})$$

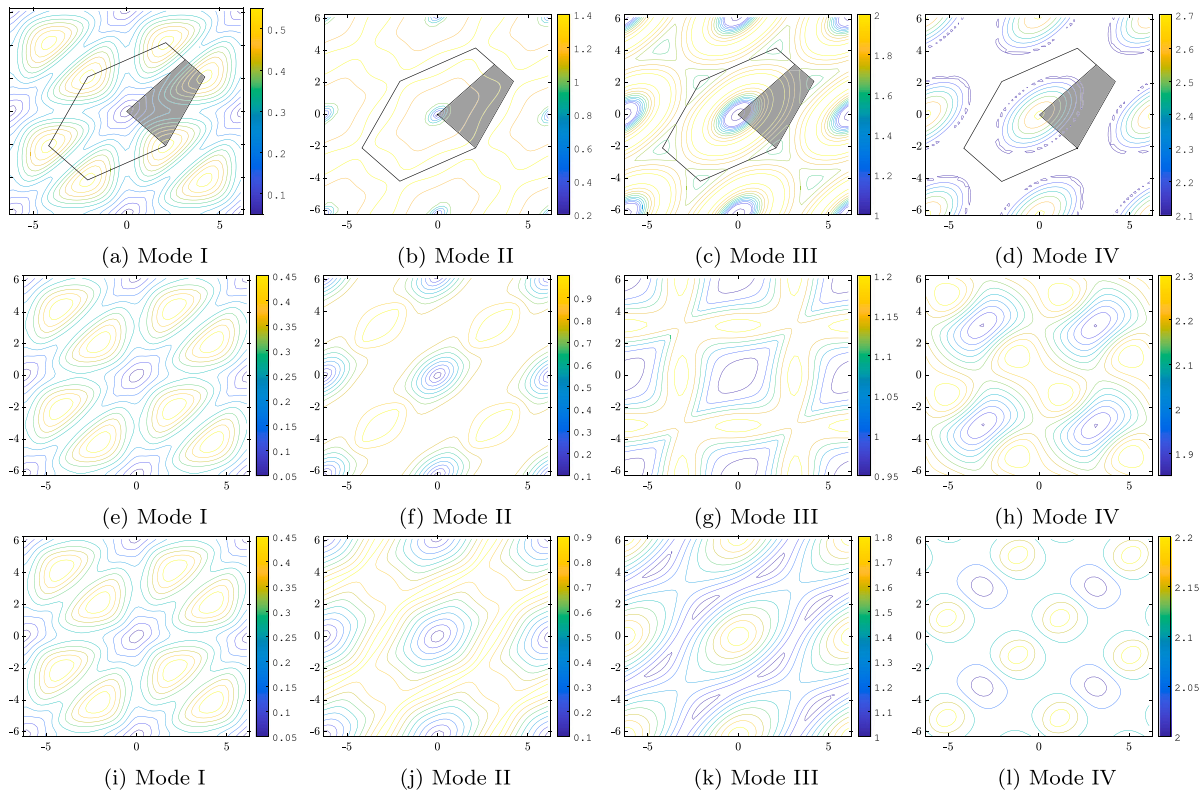


Fig. 14. Iso-frequency contour plots for the first four modes of the conventional and modified hexagonal lattice. The first row shows the contours for hexagonal lattice with straight constituent beam with $\theta = 30^\circ$. The second row shows the contour for the curved hexagonal lattice with $\theta = 30^\circ$ and $\psi_{l,r} = 50^\circ$. The third row shows the contour for the curved hexagonal lattice with $\theta = 30^\circ$ and $\psi_l = 50^\circ$, and $\psi_r = -50^\circ$.

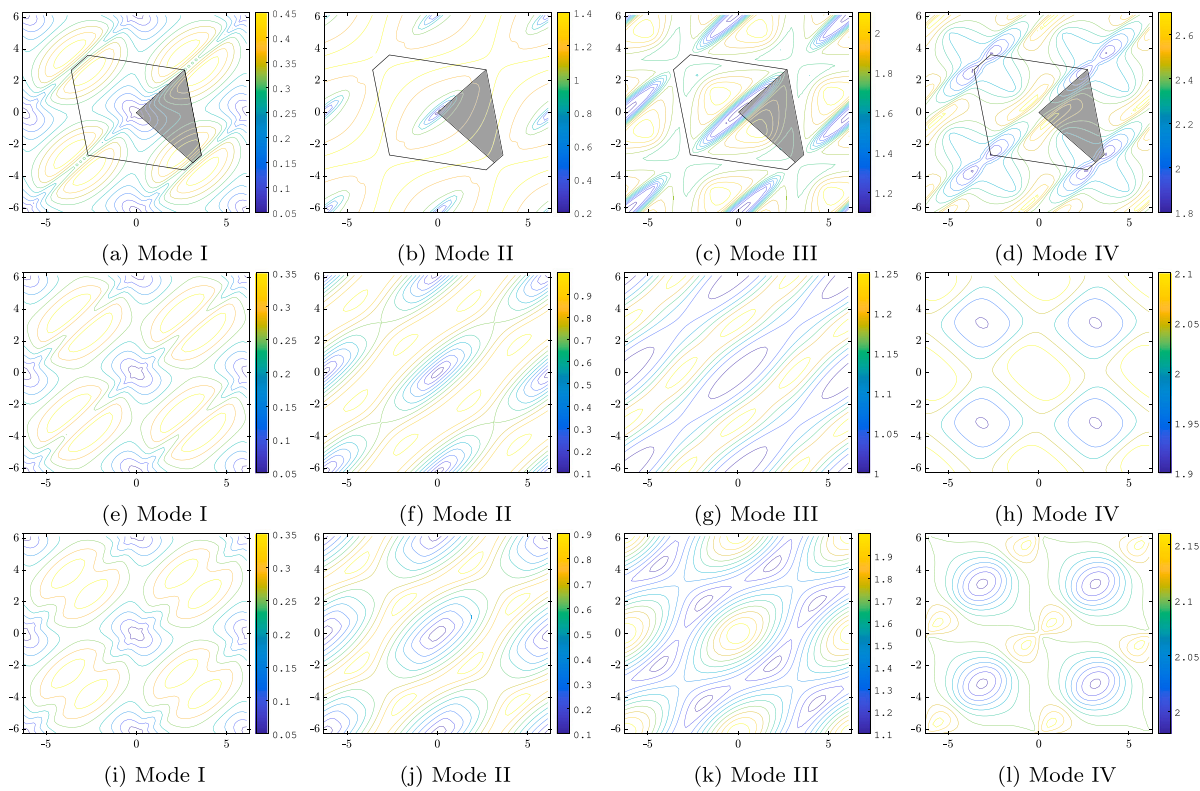


Fig. 15. Iso-frequency contour plots for the first four modes of the conventional and modified re-entrant lattice. The first row shows the contours for re-entrant lattice with straight constituent beam with $\theta = -10^\circ$. The second row shows the contour for the curved re-entrant lattice with $\theta = -10^\circ$ and $\psi_{l,r} = 50^\circ$. The third row shows the contour for the curved re-entrant lattice with $\theta = -10^\circ$ and $\psi_l = 50^\circ$, and $\psi_r = -50^\circ$.

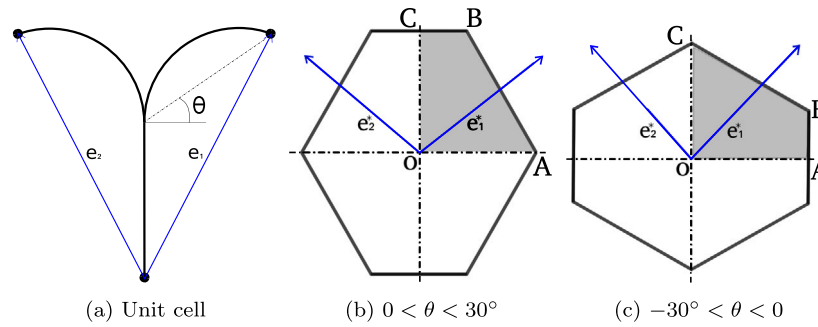


Fig. A.1. Figure showing the (a) unit cell with direct lattice vector and Brillouin zone for (b) hexagonal and (c) re-entrant lattice along with the reciprocal lattice vectors.

References

- [1] Helou M, Kara S. Design, analysis and manufacturing of lattice structures: an overview. *Int J Comput Integr Manuf* 2018;31(3):243–61.
- [2] Baravelli E, Ruzzene M. Internally resonating lattices for bandgap generation and low-frequency vibration control. *J Sound Vib* 2013;332(25):6562–79.
- [3] Iwata Y, Yokozeki T. Wave propagation analysis of one-dimensional CFRP lattice structure. *Compos Struct* 2021;261:113306.
- [4] Martinsson P, Movchan A. Vibrations of lattice structures and phononic band gaps. *Quart. J. Mech. Appl. Math.* 2003;56(1):45–64.
- [5] Ruzzene M, Scarpa F, Soranna F. Wave beaming effects in two-dimensional cellular structures. *Smart Mater Struct* 2003;12(3):363.
- [6] Spadoni A, Ruzzene M, Gonella S, Scarpa F. Phononic properties of hexagonal chiral lattices. *Wave Motion* 2009;46(7):435–50.
- [7] Gonella S, Ruzzene M. Analysis of in-plane wave propagation in hexagonal and re-entrant lattices. *J Sound Vib* 2008;312(1–2):125–39.
- [8] Zelhofer AJ, Kochmann DM. On acoustic wave beaming in two-dimensional structural lattices. *Int J Solids Struct* 2017;115:248–69.
- [9] Leamy MJ. Exact wave-based Bloch analysis procedure for investigating wave propagation in two-dimensional periodic lattices. *J Sound Vib* 2012;331(7):1580–96.
- [10] Sigmund O, Søndergaard Jensen J. Systematic design of phononic band-gap materials and structures by topology optimization. *Phil Trans R Soc A* 2003;361(1806):1001–19.
- [11] Liu W, Yoon GH, Yi B, Choi H, Yang Y. Controlling wave propagation in one-dimensional structures through topology optimization. *Comput Struct* 2020;241:106368.
- [12] An X, Fan H, Zhang C. Elastic wave and vibration bandgaps in planar square metamaterial-based lattice structures. *J Sound Vib* 2020;475:115292.
- [13] Swartz KE, White DA, Tortorelli DA, James KA. Topology optimization of 3D photonic crystals with complete bandgaps. *Opt Express* 2021;29(14):22170–91.
- [14] Gao H, Qu Y, Meng G. Topology optimization and wave propagation of three-dimensional phononic crystals. *J Vib Acoust* 2022;1–31.
- [15] Mukherjee S, Scarpa F, Gopalakrishnan S. Phononic band gap design in honeycomb lattice with combinations of auxetic and conventional core. *Smart Mater Struct* 2016;25(5):054011.
- [16] Zhang K, Su Y-c, Hou X-h, Meng J-m, Deng Z-c. Effect of pre-load on wave propagation characteristics of hexagonal lattices. *Compos Struct* 2018;203:361–72.
- [17] Bortot E, Amir O, Shmuel G. Topology optimization of dielectric elastomers for wide tunable band gaps. *Int J Solids Struct* 2018;143:262–73.
- [18] Bacigalupo A, Lepidi M, Gnecco G, Vadalà F, Gambarotta L. Optimal design of the band structure for beam lattice metamaterials. *Front Mater* 2019;6:2.
- [19] Dalkint A, Wallin M, Bertoldi K, Tortorelli D. Tunable phononic bandgap materials designed via topology optimization. *J Mech Phys Solids* 2022;163:104849.
- [20] Meng J, Deng Z, Zhang K, Xu X. Wave propagation in hexagonal and re-entrant lattice structures with cell walls of non-uniform thickness. *Waves Random Complex Media* 2015;25(2):223–42.
- [21] Cheng Q, Guo H, Yuan T, Sun P, Guo F, Wang Y. Topological design of square lattice structure for broad and multiple band gaps in low-frequency range. *Extreme Mech Lett* 2020;35:100632.
- [22] Lim QJ, Wang P, Koh SJA, Khoo EH, Bertoldi K. Wave propagation in fractal-inspired self-similar beam lattices. *Appl Phys Lett* 2015;107(22):221911.
- [23] Zhao P, Zhang K, Zhao C, Deng Z. Mechanism of band gaps in self-similar triangular lattice with koch fractal. *J Vib Acoust* 2022;144(3).
- [24] Miniaci M, Krushynska A, Movchan AB, Bosia F, Pugno NM. Spider web-inspired acoustic metamaterials. *Appl Phys Lett* 2016;109(7):071905.
- [25] Wang Y-F, Wang Y-S, Zhang C. Bandgaps and directional properties of two-dimensional square beam-like zigzag lattices. *AIP Adv* 2014;4(12):124403.
- [26] Wang Y-F, Wang Y-S, Zhang C. Bandgaps and directional propagation of elastic waves in 2D square zigzag lattice structures. *J Phys D: Appl Phys* 2014;47(48):485102.
- [27] Zhu Z, Deng Z, Huang B, Du J. Elastic wave propagation in triangular chiral lattices: Geometric frustration behavior of standing wave modes. *Int J Solids Struct* 2019;158:40–51.
- [28] Qi D, Yu H, Hu W, He C, Wu W, Ma Y. Bandgap and wave attenuation mechanisms of innovative reentrant and anti-chiral hybrid auxetic metastructure. *Extreme Mech Lett* 2019;28:58–68.
- [29] Trainiti G, Rimoli JJ, Ruzzene M. Wave propagation in undulated structural lattices. *Int J Solids Struct* 2016;97:431–44.
- [30] Zhang K, Zhao C, Zhao P, Luo J, Deng Z. Wave propagation properties of rotationally symmetric lattices with curved beams. *J Acoust Soc Am* 2020;148(3):1567–84.
- [31] Mukherjee S, Adhikari S. The in-plane mechanics of a family of curved 2D lattices. *Compos Struct* 2022;280:114859.
- [32] Fu Y, Liu W. Design of mechanical metamaterial with controllable stiffness using curved beam unit cells. *Compos Struct* 2021;258:113195.
- [33] Prasad R, Baxy A, Banerjee A. Two-dimensional in-plane elastic waves in curved-tapered square lattice frame structure. *J Appl Mech* 2022;89(3).
- [34] Karličić D, Cajić M, Chatterjee T, Adhikari S. Wave propagation in mass embedded and pre-stressed hexagonal lattices. *Compos Struct* 2021;256:113087.
- [35] Kittel C, McEuen P. *Kittel's Introduction to Solid State Physics*. John Wiley & Sons; 2018.
- [36] Perkins N, Mote Jr. C. Comments on curve veering in eigenvalue problems. *J Sound Vib* 1986;106(3):451–63.
- [37] Mace BR, Manconi E. Wave motion and dispersion phenomena: Veering, locking and strong coupling effects. *J Acoust Soc Am* 2012;131(2):1015–28.
- [38] Phani AS, Woodhouse J, Fleck N. Wave propagation in two-dimensional periodic lattices. *J Acoust Soc Am* 2006;119(4):1995–2005.
- [39] Mahajan G, Mukherjee A, Banerjee A. Influence of attached inertia and resonator on the free wave propagation in 2D square frame grid lattice metamaterial. *Waves Random Complex Media* 2021;1–28.